ANNUAL REVIEWS

Annual Review of Condensed Matter Physics

Topology and Symmetry of Quantum Materials via Nonlinear Optical Responses

J. Orenstein,[1,2] J.E. Moore,[1,2] T. Morimoto,[3] D.H. Torchinsky,[4,5] J.W. Harter,[6] and D. Hsieh[7,8]

[1]Department of Physics, University of California, Berkeley, California 94720, USA; email: jworenstein@lbl.gov

[2]Materials Sciences Division, Lawrence Berkeley National Laboratory, Berkeley, California 94720, USA

[3]Department of Applied Physics, The University of Tokyo, Hongo, Tokyo 113-8656, Japan

[4]Department of Physics, Temple University, Philadelphia, Pennsylvania 19122, USA

[5]Temple Materials Institute, Temple University, Philadelphia, Pennsylvania 19122, USA

[6]Materials Department, University of California, Santa Barbara, California 93106, USA

[7]Department of Physics, California Institute of Technology, Pasadena, California 91125, USA; email: dhsieh@caltech.edu

[8]Institute for Quantum Information and Matter, California Institute of Technology, Pasadena, CA 91125, USA

Annu. Rev. Condens. Matter Phys. 2021. 12:247–72

The *Annual Review of Condensed Matter Physics* is online at conmatphys.annualreviews.org

https://doi.org/10.1146/annurev-conmatphys-031218-013712

Keywords

photogalvanic effects, nonlinear optical effects, second-harmonic generation, LPGE, CPGE, Berry curvature, Weyl semimetals, noncentrosymmetric metals, polar metals

Abstract

We review recent progress in the study of photogalvanic effects and optical second-harmonic generation in topological and noncentrosymmetric metals.

1. INTRODUCTION

The explosion of research into the topological properties of materials has led to the realization that nontrivial phases are not at all rare, but rather ubiquitous. Rapid progress in classification of topological phases is leading to rational strategies for discovery of new topological materials (1). Furthermore, the existence of topological features in band structures, such as band-crossing points and Fermi arc surface states, has been conclusively demonstrated by angle-resolved photoemission (2–4).

An important goal of future research is to use topology to shape responses to external perturbations. A key step is to identify those effects in which band structure geometry potentially plays a key role. One class of such responses are the photogalvanic effects (PGEs), a name given to rectified photocurrents that arise in media that lack inversion symmetry (5, 6). This distinguishes PGEs from photoconductive or photovoltaic effects, where inversion symmetry is broken by the application of an external electric field or inhomogeneous chemical doping. A further distinction is that PGE-driven currents typically depend on the polarization state of the photoexcitation in a way that reflects the point–group symmetry of the medium.

Directed photocurrents in the absence of an applied electric field were first observed in the late 1960s and early 1970s (6). Controversy began early as to their origin, with a distinction emerging between intrinsic and extrinsic mechanisms. Intrinsic PGE response functions can in principle be calculated directly from the electron energies and wave functions. Whereas the standard perturbation theory treatment of intrinsic PGE mechanisms is generally valid, the emergence of geometric quantities such as the Berry curvature of Bloch states gives new insights into the source of these effects and features such as approximate quantization. However, extrinsic sources of PGEs involve electron and phonon scattering processes that are beyond the scope of band structure calculations. In many ways the problem of separating intrinsic versus extrinsic contributions to PGEs mirrors the analogous problem regarding the anomalous Hall effect (AHE), which took many decades to resolve (7). As the purpose of this review is to present PGEs as a probe of topological phases and interfaces, we focus mainly on intrinsic mechanisms. However, we hope that it also serves to motivate studies of PGEs as a function of temperature and disorder, as such research played a key role in resolving the long-running controversy as to the origin of the AHE.

A nonlinear response that is closely related to PGEs is optical second-harmonic generation (SHG), a frequency doubling of light through interaction with media that lack inversion symmetry (8). Although the manifestations of band topology are not as direct in SHG as they are in PGEs, the former plays a key role in understanding the nature of noncentrosymmetric metals, the systems in which most topological band structures are found. The very existence of noncentrosymmetric metals is counterintuitive because itinerant electrons tend to screen local electric dipole moments and inhibit their cooperative ordering. Indeed, the vast majority of known metals have centrosymmetric structures. The possibility of stabilizing such materials by decoupling itinerant electrons from an inversion breaking structural mode was theoretically proposed over 50 years ago by Anderson & Blount (9), but uncovering the microscopic pathways that lead to this phenomenon remains a subject of intensive study (10–12). The noncentrosymmetric metallic compounds at the heart of present topological materials studies already lack inversion symmetry under ambient conditions. We describe how the SHG responses of a rare class of spontaneous noncentrosymmetric metals, which break inversion only upon cooling, can lend insight into this problem and potentially lead to new pathways for discovering topological materials.

The outline of this review is as follows. The introduction gives a brief guide to the classification of PGEs and how the response tensors are influenced by the crystal symmetry. Sections 1 and 2 describe the theory of intrinsic PGEs in the intra- and interband regimes. Sections 3 and 4 present

an overview of relevant experiments in these two regimes. Section 5 discusses the principles and applications of SHG for studying spontaneous noncentrosymmetric metals. Finally, we conclude with a short perspective on future directions.

1.1. Taxonomy of Effects

Associated with PGEs are a large and sometimes redundant set of descriptors, classifying them according to pump wavelength, polarizations, and underlying mechanisms. Below we provide a brief guide to the naming schemes found in the PGE literature.

1.1.1. Linear photogalvanic effect versus circular photogalvanic effect. Categorizing PGEs begins with the polarization state of the photons that induce the current. The linear photogalvanic effect (LPGE) is observed with linearly polarized light, whereas the circular photogalvanic effect (CPGE) refers to the difference in photocurrent observed when the polarization state of the pump field is switched between left and right circular polarization.

Although both effects require inversion breaking, the origins of the CPGE and LPGE are fundamentally different, as anticipated from the fact that circular photoexcitation breaks time reversal in the same sense as an applied magnetic field. The inverse Faraday effect, in which circularly polarized light generates a magnetization by selectively pumping one direction of angular momentum, is an intuitive example of this similarity between circularly polarized light and a magnetic field (13).

1.1.2. Intrinsic versus extrinsic. A second distinction is between photocurrent associated with photogeneration of electron–hole pairs, as opposed to their subsequent scattering and recombination. The photogeneration mechanism is intrinsic in the sense that the photocurrent can, in principle, be calculated directly from electron energy eigenstates, without reference to kinetic factors such as electron–phonon or electron–impurity scattering rates. Once created, the scattering and recombination of photogenerated electron–hole pairs can induce an additional contribution to the photocurrent, which we refer to as extrinsic.

Extrinsic PGE arises from the violation of detailed balance that emerges when either inversion or time-reversal symmetries are broken. Detailed balance is the presumed equality of transition probabilities for forward and reverse transitions between two states. In the context of crystal physics the relevant states are eigenstates of momenta, k_1 and k_2, in which case detailed balance corresponds to $\Gamma_{k_1,k_2} = \Gamma_{k_2,k_1}$. These transition probabilities, Γ, are the squared moduli of matrix elements, M_{k_1,k_2}, which have the property that $M_{k_1,k_2} = M^*_{k_2,k_1}$. However, the microscopic reversibility of matrix elements is not sufficient to ensure detailed balance. In fact, both time-reversal, $M_{k_1,k_2} = M^*_{-k_2,-k_1}$, and inversion symmetry, $M_{k_1,k_2} = M_{-k_2,-k_1}$, are required to ensure $\Gamma_{k_1,k_2} = \Gamma_{k_2,k_1}$. In a crystal in which either inversion or time reversal is broken, the rate of scattering directly from $\mathbf{k}$ to $-\mathbf{k}$ is not equal to the rate from $-\mathbf{k}$ to $\mathbf{k}$. As a result, a nonequilibrium distribution of electron–hole pairs can acquire a net current in the process of returning to equilibrium via scattering and recombination. Indeed, as emphasized by Belinicher & Sturman (5), scattering- and recombination-driven photocurrent must be present to ensure that the net photocurrent is zero when the crystal is exposed to thermal radiation at its equilibrium temperature.

1.1.3. Interband versus intraband. The last distinction is between intraband and interband contributions to PGEs. In the intraband case, which is specific to metallic phases, the photoexcitation frequency lies within the Drude absorption band. In the absence of scattering, the Drude optical conductivity approaches a δ function at zero frequency; intraband absorption for $\omega > 0$

requires phonon, impurity, or electron–electron scattering on a lattice to conserve momentum. As a result, the intraband PGE cannot be purely intrinsic; i.e., it cannot be predicted solely on the basis of band structure geometry. However, treating the intraband regime using semiclassical dynamics yields an elegant physical picture of PGEs arising from the interplay between finite momentum lifetime and Berry curvature.

In contrast with intraband absorption, momentum conserving (vertical) transitions are allowed in the absence of disorder. Consequently, a purely intrinsic mechanism exists, and the PGE amplitude and spectrum can in principle be calculated from the electron eigenfunctions, at least in the noninteracting limit. In the case of the LPGE, the exact Kubo formula expression has been interpreted in terms of a quantity called the shift vector, $\mathbf{R}(\mathbf{k})$ (14), which when averaged over the Brillouin zone can be related to the relative polarization of the bands (15). The CPGE can be directly related in some cases to the gauge-invariant Berry curvature of the bands involved in the optical transition. In an idealized model of a Weyl semimetal, the CPGE is in fact quantized, proportional only to the Berry monopole charge of the Weyl node and fundamental constants. Although precise quantization is not protected with respect to disorder and interactions, the CPGE in Weyl semimetals is perhaps the only example of a nearly universal topological quantity in metallic phases and in nonlinear optics as well.

1.2. Symmetry Considerations

To linear order, time-varying optical electric fields induce time-varying currents at the same frequencies. New frequencies, corresponding to the sum and difference of the driving frequencies, appear at second order in the applied field. In its most general form, the second-order current is expressed in terms of a third-rank tensor, σ_{ijk}:

$$\mathbf{J}_i(\omega_1 \pm \omega_2) = \sigma_{ijk}(\omega_1 \pm \omega_2; \omega_1, \omega_2)[E_j(\omega_1) + E_j(-\omega_1)][E_k(\omega_2) + E_k(-\omega_2)]. \quad 1.$$

As $\mathbf{J}$ is odd under spatial inversion, whereas E^2 is even, all second-order responses vanish in centrosymmetric media.

For PGEs, we consider monochromatic excitation at frequency ω such that difference frequency generation yields a zero-frequency current, $\mathbf{J}_{\mathrm{dc}}$. The PGE current is proportional to $E_j(\omega)E_k(-\omega)$, or equivalently $E_j(\omega)E_k^*(\omega)$, and therefore σ_{ijk} and σ_{ikj} are independent tensor elements if $k \neq j$. This contrasts with SHG, which denotes a current at twice the excitation frequency, $\mathbf{J}_{2\omega}$. Because the SHG current is proportional to $E_j(\omega)E_k(\omega)$, the response tensor exhibits intrinsic permutation symmetry, such that σ_{ijk} is equivalent to σ_{ikj}. As a consequence, unlike the PGE, SHG cannot sense chirality of the crystal structure.

Unlike the second-harmonic current, the PGE amplitude in the formalism must be a real vector, as it corresponds to a zero-frequency response. If we separate the PGE components with $j = k$ and $j \neq k$, we can write

$$\mathbf{J}_i(0) = \sigma_{ijj}|E_j|^2 + \sigma_{ijk}E_jE_k^* + \sigma_{ikj}E_j^*E_k, \quad 2.$$

from which it follows that the reality of $\mathbf{J}_i$ implies that the σ_{ijj} are real and that $\sigma_{ijk} = \sigma_{ikj}^*$. To clarify the role of crystal symmetry, it is useful to separate the real and imaginary terms in the conductivity tensor like so:

$$\mathbf{J}_i(0) = \sigma_{ijj}|E_j|^2 + \mathrm{Re}\{\sigma_{ijk}\}(E_jE_k^* + E_j^*E_k) + i\beta_{ij}(\mathbf{E} \times \mathbf{E}^*)_j, \quad 3.$$

where $\beta_{ij} = \epsilon_{jkl}\sigma_{ikl}$. The terms proportional to β_{ij} are odd under the transformation $\omega \to -\omega$ or equivalently $t \to -t$, whereas the other terms are even.

The current that corresponds to the real and imaginary components of σ_{ijk} are distinguished by their response to polarized light. For linear polarization, the helicity vector $\mathbf{E} \times \mathbf{E}^*$ is equal to zero; the photocurrent corresponding to the first two nonzero terms in Equation 3 is known as the LPGE. Conversely, for circular polarization only the last term is nonzero and the resulting current is the CPGE. Note that the CPGE current reverses sign under complex conjugation of the electric field, which is equivalent to changing polarization from left to right circular.

The LPGE and CPGE tensors that describe the bulk crystal response follow in general from the point–group symmetry of the crystal. The real components of σ_{ijk} transform as a symmetric polar rank-three tensor, whereas β_{ij} is an axial rank-two tensor. The CPGE tensor β_{ij} has the same structure as the gyromagnetic tensor α_{ij} that relates current to applied magnetic field through the gyromagnetic effect, $\mathbf{J}_i = \alpha_{ij} B_j$. That this connection should exist is clear from the fact that $\mathbf{E} \times \mathbf{E}^*$ is an axial vector having the same symmetry properties as $\mathbf{B}$. Note that both the GME and CPGE tensors vanish in the limit that $\omega \to 0$.

2. INTRABAND MECHANISMS RELATED TO BAND STRUCTURE GEOMETRY

Historically, the first physical picture for intrinsic CPGE was based on the phenomenon of optical spin orientation (16). Near high-symmetry points in the Brillouin zone electron eigenstates can be approximate eigenfunctions of total angular momentum $\mathbf{J}$. Breaking of inversion symmetry leads to linear in $\mathbf{k}$ spin–momentum coupling terms and nondegenerate spin–split bands. In the case of intraband excitation of quantum wells, circularly polarized light can generate a net electrical current through spin-selective virtual transitions involving states in different 2D subbands (17).

The picture described above relies on the existence of electron subbands with well-defined spin and strong spin–momentum coupling. However, it was subsequently found that CPGE with comparable magnitude can also be found in Si metal–oxide–semiconductor field-effect transistor (MOSFET) structures (18). Because the spin–momentum coupling in Si is negligible, the picture of virtual transitions between spin–split subbands is not applicable. Thus, these observations suggest a more general underlying physical picture for the origin of intrinsic intraband CPGE.

2.1. Berry Curvature

Berry curvature provides a physical basis for CPGE in the intraband regime that includes spin orientation and virtual interband transitions as a special case. In this picture, PGEs result from the anomalous velocity induced by Berry curvature (19). To see the origin of this effect, we first define Berry curvature in the context of crystal band structure. The curvature of an electron band in momentum space is related to how Bloch functions vary with infinitesimal changes in momentum. Although one might imagine the curvature would be related to the overlap of Bloch functions at nearby points in momentum space, this is not quite right, as $\langle u(k_0)|u(k_1)\rangle$ is not gauge invariant.

However, the product of such overlaps around a closed contour C in momentum space is gauge invariant (20). The phase accumulated in the limit of infinitesimal step size is the Berry phase, γ_{B}, which can be written as

$$\gamma_{\mathrm{B}} = \Phi = \int_S \mathbf{\Omega}(\mathbf{k}) \cdot \mathrm{d}\mathbf{S}, \qquad 4.$$

where S denotes the surface encircled by C and $\mathrm{d}\mathbf{S}$ denotes the surface element. This defines Berry curvature, $\mathbf{\Omega}(\mathbf{k})$. The Berry curvature thus defined in the momentum space is analogous to the magnetic field in electromagnetic theory (21). We collect the basic Berry phase quantities in the sidebar titled Berry Phase Expressions for ready reference.

BERRY PHASE EXPRESSIONS

Many properties of solids are governed at low energies by certain geometrical objects that capture how the periodic part $u(\mathbf{k})$ of Bloch wave functions evolves with crystal momentum $\mathbf{k}$. The Berry connection

$$\mathbf{a}(\mathbf{k}) = i\langle u(\mathbf{k})|\partial_{\mathbf{k}} u(\mathbf{k})\rangle$$

forms the integrand of the Berry phase γ_B, the geometric phase acquired when the wave function evolves around a closed-loop C in momentum space:

$$\gamma_B = \oint_C \mathbf{a}(\mathbf{k}) \cdot \mathrm{d}\mathbf{k}.$$

The Berry connection is not invariant under a change of phase $|u(\mathbf{k})\rangle \rightarrow e^{i\chi(\mathbf{k})}|u(\mathbf{k})\rangle$, but changes by the gradient of the phase χ, much like the vector potential in electromagnetism. But an invariant object is the Berry curvature, defined as the momentum-space curl of the Berry connection,

$$\boldsymbol{\Omega}(\mathbf{k}) = \nabla_{\mathbf{k}} \times \mathbf{a}(\mathbf{k}),$$

and numerous physical properties are now understood to depend on $\boldsymbol{\Omega}(\mathbf{k})$.

2.2. Anomalous Velocity

In the semiclassical regime, the band structure geometry acts through the Berry curvature to generate a transverse motion of an accelerating electron wave packet, which is known as the anomalous velocity, $\mathbf{v}_{an}$. A physical picture (22) of $\mathbf{v}_{an}$ is presented in **Figure 1**, which illustrates the propagation of a slice of an electron wave packet in the presence of an electric field in the x direction. Viewed in momentum space (**Figure 1*a***), k_x advances by $eE_x\delta t/\hbar$ in time interval δt. The change in the phase of the wave function around a contour defined by the small patch of dimension $\mathrm{d}k_x \times \mathrm{d}k_y$ is given by the flux of the Berry curvature,

$$\mathrm{d}\gamma_B = \left[\Omega_z(\boldsymbol{k})\frac{eE_x \mathrm{d}t}{\hbar}\right]\mathrm{d}k_y. \qquad 5.$$

The relationship between phase and displacement for wave packet propagation, $\mathrm{d}y = \mathrm{d}\gamma_B/\mathrm{d}k_y$, leads to a velocity transverse to the electric field given by $\dot{y} = eE_x\Omega_x(\mathbf{k})/\hbar$ which is depicted in real space in **Figure 1*b***.

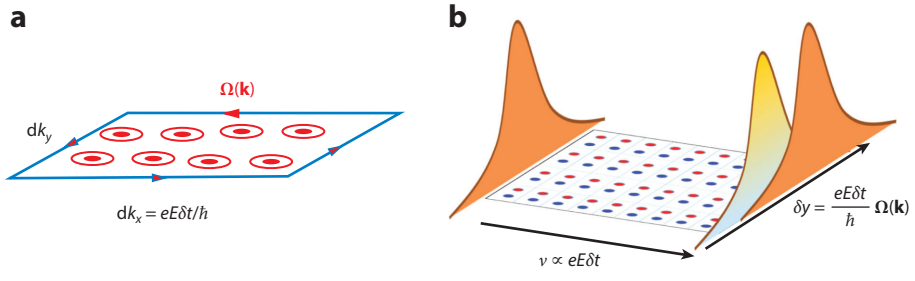

Figure 1

Physical picture of anomalous velocity related to Berry curvature. (*a*) Infinitesimal area in momentum space whose contour is defined by the electric-field-induced increase in k_x in time δt and an element of transverse momentum, $\mathrm{d}k_y$. (*b*) Corresponding wave packet propagation in real space.

2.3. Berry Curvature and Intrinsic Nonlinearity

The conditions for nonzero Berry curvature follow from its properties under time-reversal and inversion symmetry (21):

$$\begin{aligned} \text{Inversion symmetry:} \quad & \boldsymbol{\Omega}(\mathbf{k}) = \boldsymbol{\Omega}(-\mathbf{k}) \\ \text{Time-reversal symmetry:} \quad & \boldsymbol{\Omega}(\mathbf{k}) = -\boldsymbol{\Omega}(-\mathbf{k}) \end{aligned} \qquad 6.$$

It follows from Equation 6 that breaking either time-reversal or inversion symmetry is a necessary condition for nonzero Berry curvature, $\boldsymbol{\Omega}(\mathbf{k})$. In T breaking systems, $\boldsymbol{\Omega}(\mathbf{k})$ is an even function of momentum; consequently the anomalous velocity averaged over an equilibrium distribution of occupied states is nonzero. As a result, the effects of time-reversal breaking are manifest in linear response functions such as the AHE and the quantized spin Hall effect in Chern insulators. In particular, the AHE is proportional to the flux of $\boldsymbol{\Omega}(\mathbf{k})$ through the equilibrium Fermi surface (FS). By contrast, the Berry curvature is odd in momentum in systems that break inversion but preserve time-reversal symmetry. Here, T symmetry ensures that the average anomalous velocity, or equivalently, the flux of Berry curvature through any iso-energy contour is zero in equilibrium.

Although not exhibiting an AHE, the antisymmetric Berry curvature in broken inversion systems is a gauge-invariant quantity that should be observable. The signature response of systems that break inversion symmetry is the appearance of current proportional to E^2, and this suggests there is a link between the second-order nonlinear conductivity and the antisymmetric $\boldsymbol{\Omega}(\boldsymbol{k})$. This link was demonstrated in References 23–25, where it was shown that, indeed, σ_{ijk} reveals the presence of a hidden Berry curvature that cannot be seen in linear response.

To see how this comes about, consider a two-dimensional crystal with a single mirror plane M_x that maps $x \to -x$. As the symmetry $y \to -y$ is broken, the structure lacks inversion symmetry. For the z component of the Berry curvature, time-reversal symmetry enforces $\Omega_z(k_x, k_y) = -\Omega_z(-k_x, -k_y)$, whereas the mirror symmetry enforces $\Omega_z(k_x, k_y) = -\Omega_z(-k_x, k_y)$. Thus Ω_z must be an even function of k_y and an odd function of k_x. As we have stated previously, the flux through the equilibrium FS is zero, as is the AHE. However, if the FS is displaced in the direction of k_x by an electric field, then the flux will be nonzero. For purposes of illustration we assume that the curvature is small such that $\Omega_z(k_x) = \beta k_x$ is a good approximation.

Consider circular polarization $\mathbf{E}(t) = E_0(\mathbf{x}\cos\omega t \pm \mathbf{y}\sin\omega t)$ and assume the low frequency limit of intraband transport in which $\omega \ll 1/\tau$, where τ is the momentum relaxation time. In this limit, the displacement of the FS is parallel to the instantaneous electric field. The net flux $\Phi(t)$ through the displaced FS is time dependent and is proportional to $\beta E_0 \tau \cos\omega t$. The nonzero flux drives an anomalous current, $\mathbf{J} = \boldsymbol{\delta}\dot{\mathbf{k}}(t) \times \Phi(t)\mathbf{z}$, where the instantaneous acceleration is given by $\boldsymbol{\delta}\dot{\mathbf{k}}(t) = e\mathbf{E}\omega\tau/\hbar(-\mathbf{x}\sin\omega t \pm \mathbf{y}\cos\omega t)$.

Substituting the acceleration into the expression for the anomalous current yields a DC current in the x direction proportional to the second power of the applied electric field. The direction of the current reverses with reversal of the sense of circular polarization of the excitation field,

$$\mathbf{J}_{\rm dc} = \pm\mathbf{x}\frac{\beta n e^3}{2\hbar^2}\omega\tau^2 E_0^2, \qquad 7.$$

corresponding to the CPGE.

Sodemann & Fu (24) generalized this idea to arbitrary antisymmetric $\boldsymbol{\Omega}(\mathbf{k})$ and higher dimensions. For example, in three dimensions, the anomalous current is given by

$$\mathbf{J} = e\dot{\mathbf{k}} \times \int d^3k\, f(\mathbf{k})\boldsymbol{\Omega}(\mathbf{k}), \qquad 8.$$

where $f(\mathbf{k})$ is the fermion occupation function and $\dot{\mathbf{k}} = e\mathbf{E}/\hbar$ is the instantaneous acceleration. Because the Berry curvature is odd in momentum, the integral in Equation 8 is proportional to the steady state displacement of the FS as a result of the applied field $\delta\mathbf{k}$,

$$\mathbf{J} = (e^2/2\hbar)\mathbf{E} \times \int d^3k \nabla_k f(\mathbf{k}) \cdot \delta\mathbf{k}\, \boldsymbol{\Omega}(\mathbf{k}). \quad 9.$$

If we include the effect of finite frequency in the relaxation time approximation, then $\delta\boldsymbol{k} = (e\mathbf{E}\tau/\hbar)/(1 + i\omega\tau)$. To see how Equation 9 translates to the second-order conductivity tensor, we can evaluate, for example, the z-directed current resulting from an electric field in the x direction, which is given by the σ_{zxx} component. Substitution of $\mathbf{E} = E\mathbf{x}$ into Equation 9 yields

$$\sigma_{zxx} = \frac{e^3\tau/2\hbar^2}{(1 + i\omega\tau)} \int d^3k \frac{\partial f}{\partial k_x} \Omega_y = \frac{e^3\tau/2\hbar^2}{(1 + i\omega\tau)} \int d^3k f_0 \frac{\partial \Omega_y}{\partial k_x}, \quad 10.$$

where the second equality follows from integration by parts and f_0 is the equilibrium occupation function. Sodemann & Fu (24) showed that the full nonlinear response tensor can be written in the form,

$$\sigma_{abc} = \frac{e^3\tau/2\hbar^2}{(1 + i\omega\tau)} \epsilon_{adc} D_{bd}, \quad 11.$$

where D_{ij} was termed the Berry curvature dipole (BCD) and given by

$$D_{ij} \equiv \int_k f_0 \frac{\partial \Omega_j}{\partial k_i}. \quad 12.$$

The BCD compactly expresses the intrinsic semiclassical response in terms of an axial tensor of rank $3 - d$, where d is the dimensionality of the system. In two dimensions, where the Berry curvature becomes a pseudoscalar and the BCD is an axial vector, $\mathbf{D}$, the photogalvanic current takes an especially simple form,

$$\mathbf{J} = \frac{e^3\tau/2\hbar^2}{(1 + i\omega\tau)} \hat{\boldsymbol{z}} \times \mathbf{E}^*(\mathbf{D} \cdot \mathbf{E}). \quad 13.$$

Equation 13 reproduces the results derived previously in Reference 23, where a Berry curvature that is linear in wave vector was chosen for illustrative purposes.

Note that the current is purely transverse to the applied electric field as a consequence of its origin in the anomalous velocity. Furthermore, Equation 13 describes both LPGE and CPGE currents. If we take $\mathbf{D}$ to be parallel to the x axis, then, the magnitude of the LPGE current as the direction of linear polarization sweeps through an angle θ is given by,

$$|\mathbf{J}_{\mathrm{LPGE}}| = E^2 \frac{e^3\tau}{2(1 + \omega^2\tau^2)} D \cos^2\theta. \quad 14.$$

If instead the current is generated by circular polarization, then the CPGE current flows parallel to $\mathbf{D}$ and is given by,

$$\mathbf{J}_{\mathrm{CPGE}} = E^2 \frac{e^3\omega\tau^2}{2(1 + \omega^2\tau^2)} \mathbf{D}. \quad 15.$$

The CPGE current in the limit that $\omega \gg 1/\tau$ approaches an intrinsic value that depends only on the band structure geometry as embodied in the BCD. In the opposite limit, CPGE vanishes as expected because the distinction between left and right circular is a property of time-dependent fields. In contrast, LPGE approaches a nonzero value as $\omega \to 0$, and this dc response is referred to as the nonlinear Hall effect (NHE).

3. QUANTUM DYNAMICS: TOPOLOGICAL NONLINEAR PHOTONICS AND THE QUANTIZED PHOTOGALVANIC EFFECT

In this section, we overview nonlinear optical effects in which the photon energy is above the band gap and the light irradiation leads to photoexcitation of electron–hole pairs. As the semiclassical picture relates Berry curvature to the anomalous velocity of a single band, it might seem unlikely that Berry physics plays a role when interband transitions are involved. However, it has been revealed in the past decades that important nonlinear optical effects including shift currents and injection currents are probes of the band structure geometry (26–31). Below, we give a brief review of theories on geometric nonlinear optical effects in the interband regime.

Shift current: photocurrent induced by shift of electron wave packet upon interband photoexcitation; induces LPGE under T symmetry

Injection current: photocurrent induced by group velocity of photoexcited electrons and holes; grows linearly in time and induces CPGE under T symmetry

3.1. Formalism of Second-Order Nonlinear Optical Effects in the Interband Regime

A general formalism for LPGE and CPGE has been established by Sipe & Shkrebtii (26). The nonlinear conductivity, $\sigma_{ijk}(0; \omega, -\omega)$, for the dc current response can be decomposed into two pieces: (*a*) shift current and (*b*) injection current. In the presence of time-reversal symmetry, shift current corresponds to LPGE and injection current to CPGE. Physically, shift current is associated with a change in the position of the electron wave packet upon photoexcitation from the valence to conduction band. The momentum-resolved change in an intracell coordinate is described by shift vector $\boldsymbol{R}(\boldsymbol{k})$, which is the difference in the gauge-covariant derivative of the Bloch functions of the two bands. The shift current arising in ferroelectrics such as $BaTiO_3$ has been studied by using first-principle calculations (27, 28, 32).

The relationship between LPGE and band structure geometry is somewhat tenuous, as the physically observable nonlinear conductivity involves an integral of $\boldsymbol{R}(\boldsymbol{k})$ over momentum, weighted by dipole matrix elements. Below, we focus on injection current, or CPGE, where the relationship to band structure geometry and topology is more direct. The injection current is induced by free motion of photoexcited electrons and holes according to their group velocities and, in the absence of momentum relaxation, grows linearly $\mathfrak{d}$ in time under continuous light irradiation.

An expression for the CPGE current, $\dot{\mathbf{J}}_i = \beta_{ij}(\mathbf{E} \times \mathbf{E}^*)_j$, can be obtained directly from Fermi's golden rule (26, 33),

$$\beta_{ij} = \frac{\pi e^3}{\hbar}\epsilon_{jkl}\int [\mathrm{d}k] \sum_{n,m} f_{nm}\Delta^i_{nm} r^k_{nm} r^l_{mn}\delta(\hbar\omega - E_{mn}), \qquad 16.$$

where ϵ_{jkl} is the antisymmetric tensor, $[\mathrm{d}k] \equiv \mathrm{d}\mathbf{k}/(2\pi)^3$, $f_{nm} = f_n - f_m$ with Fermi distribution function f_n for the band n, $r^i_{nm} = i\langle n|\partial_{\boldsymbol{k}}|m\rangle$ is the interband Berry connection for the bands n and m, $E_{nm} = E_n - E_m$ with the band dispersion E_n for the band n, and $\Delta^i_{nm} = \partial_{k_i}E_{nm}/\hbar$. The δ function specifies the k points, where energy conserving transitions take place from the band n to m. The transition rates are given by matrix elements $|(r^k \pm ir^l)_{mn}|^2$ for left and right circular polarization. The difference of transition rates, which leads to the CPGE amplitude, is the cross term $\epsilon_{jkl}r^k_{nm}r^l_{mn}$. The photoexcited electrons and holes carry net current proportional to the difference of their group velocities, Δ^i_{nm}. Combining these terms and integrating over the Brillouin zone, we obtain the formula Equation 16.

The CPGE has a direct relationship to Berry curvature in two band systems, which is given by $\Omega^c = i\epsilon_{abc}r^a_{\mathrm{vc}}r^b_{\mathrm{cv}}$, where v and c indicate the valence and conduction bands, respectively. Using this

equation, we can rewrite Equation 16 as

$$\beta_{ij} = \frac{i\pi e^3}{\hbar^2} \int [\mathrm{d}k] \partial_{k_i} E_{\mathrm{vc}} \Omega^j \delta(\hbar\omega - E_{\mathrm{cv}}), \qquad 17.$$

which shows that CPGE is governed by the Berry curvature in the two band limit. We note that the presence of momentum relaxation gives a cutoff for the growth of current response in time. In the steady state, the current is given by $\mathbf{J}_i = \beta_{ij}\tau(\mathbf{E} \times \mathbf{E}^*)_j$ with the relaxation time τ.

The relationship between Berry curvature and interband CPGE was first pointed out by Hosur for the surface Dirac states of topological insulators (34). The surface of topological insulators such as Bi_2Se_3 hosts massless Dirac fermions with hexagonal warping that support nonzero Berry curvature. However, the threefold symmetry of Bi_2Se_3 forbids in-plane current at the normal incidence, and the C_3 symmetry must be broken by an external perturbation such as magnetic field or strain to observe CPGE from the 2D surface states of topological insulators.

3.2. Quantized Circular Photogalvanic Effect in Weyl Semimetals

The topological nature of CPGE has a more direct manifestation in 3D Weyl semimetals (33), potentially allowing direct access to the topological charge of Weyl fermions through an optical probe. **Figure 2*a*,*b*** illustrates the origin of CPGE for an idealized Weyl node, characterized by a linear and isotropic dispersion. The sphere surrounding the Weyl cone in **Figure 2*a*** is a surface constant energy, with arrows representing both the local pseudospin and Berry curvature direction. For this simplified model, the locus of points in $\boldsymbol{k}$ space connected by vertical transitions at some energy $\hbar\omega$ is also a sphere centered on the Weyl node, as shown in **Figure 2*b***. Such transitions take place between states with opposite pseudospin. As is clear from the schematic, the sense of circular polarization that flips a pseudospin from down to up preferentially induces transitions in the "Northern Hemisphere," generating a net current in the direction of the "North Pole" (and vice versa for light of opposite helicity).

With this physical picture in mind, we can return to mathematics to derive quantization of the CPGE current. The trace of β_{ij}, derived from Equation 17, can be rewritten in terms of the Berry flux,

$$\mathrm{tr}[\beta] = i\frac{e^3}{2h^2} \int_S \boldsymbol{\Omega} \cdot \mathrm{d}\mathbf{S}, \qquad 18.$$

where the surface S is the locus of energy conserving transitions in momentum space and $\mathrm{d}\mathbf{S}$ denotes an element of that surface. In this situation, $\int_S \boldsymbol{\Omega} \cdot \mathrm{d}\mathbf{S}$ becomes nothing but the topological charge of the Weyl fermion, and CPGE exhibits quantization corresponding to the Weyl charge C as

$$\mathrm{tr}[\beta] = i\pi \frac{e^3}{h^2} C. \qquad 19.$$

Note that the linear, isotropic dispersion that we used to illustrate the physical origin of CPGE is not necessary for quantization, which requires only that S be a closed surface encircling the Weyl point.

Although each Weyl node contributes a quantum of CPGE, this direct signature of topological charge can be hidden. The Nielsen–Ninomiya no-go theorem requires the total monopole charge in the Brillouin zone to be zero (37). In systems that retain mirror symmetry, nodes of opposite charge are degenerate in energy, leading to an exact cancellation of the trace of β_{ij}. Despite this, off-diagonal terms of β_{ij} can be nonzero in mirror symmetric Weyl semimetals such as TaAs as a consequence of tilting of the Weyl cones (38). However, in such systems the CPGE amplitude

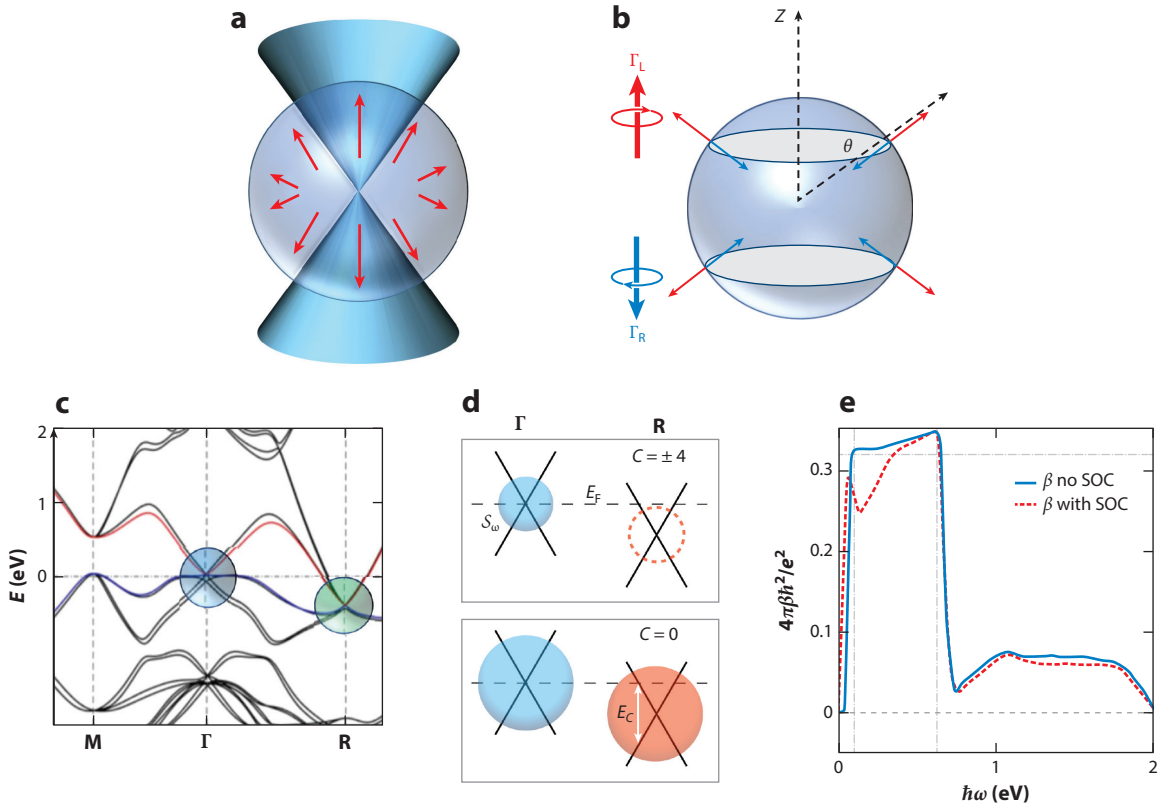

Figure 2

Quantized CPGE. (*a*) Illustration of Weyl dispersion, showing a surface of constant energy and the direction of electron pseudospin and Berry curvature. (*b*) Sphere in momentum space indicating the locus of $\boldsymbol{k}$-points for energy-conserving optical transitions. Arrows indicate the pseudospin vectors of occupied (*blue*) and unoccupied (*red*) states; transitions between them are generated by circularly polarized light, depicted as vertical arrows. (*c*) Locations of Weyl nodes with opposite Berry monopole charge in RhSi band structure. Panel adapted from Reference 35. (*d*) Evolution of the surface of allowed transitions with photon energy, showing the transition from Chern number four to zero as the Pauli blocking energy is exceeded. (*e*) Prediction of quantized CPGE in RhSi, showing a plateau in CPGE amplitude and a cutoff at the Pauli blocking energy. Panel adapted from Reference 36. Abbreviations: CPGE, circular photogalvanic effect; SOC, spin-orbit coupling.

is not a topological property directly related to the Berry monopole charge through fundamental constants.

The properties of chiral Weyl semimetals, in which all mirror symmetries are broken, are qualitatively different from mirror preserving materials such as TaAs. In chiral Weyl semimetals, nodes with opposite topological charge need not be degenerate in energy. Thus, it is possible for one node to lie near the Fermi energy, E_F, while its oppositely charged partner is below. Transitions near the node below E_F are Pauli blocked at sufficiently low photon energy, and a quantized CPGE (QCPGE) arising from the Weyl node near E_F emerges (33).

RhSi and closely related isostructural chiral compounds have been proposed as ideal candidates to exhibit a QCPGE (35, 39). These are multifold-fermion, rather than Weyl, semimetals, as their theoretical band structure exhibits gapless excitations with greater than twofold degeneracy at band-crossing points. Their low-energy excitations can be described by a Hamiltonian $H = v_F \mathbf{k} \cdot \mathbf{S}$ with $\mathbf{S}$ being a higher spin representation of SU(2) with $S = 1, 3/2, 2, \ldots$. Like

Weyl nodes, multifold gapless points behave as sinks and sources of Berry flux, leading to quantization of CPGE in the same manner (39), but with higher Chern number. The prediction of multifold-fermion dispersion and exotic Fermi arcs (35, 40) was confirmed recently by ARPES (angle-resolved photoemission spectroscopy) measurements in RhSi and CoSi (41–43).

As shown in **Figure 2*c***, density functional theory (DFT) applied to RhSi predicts a large energy difference between Weyl points of opposite charge at Γ and *R*, such that the regime of Pauli blocking extends to $\hbar\omega \sim 0.65$ eV. **Figure 2*d*** illustrates the evolution of the surface, $\mathbf{S}_\omega$, in $\mathbf{k}$ space defined by the optical transitions at energy $\hbar\omega$. For sufficiently small $\hbar\omega$, $\mathbf{S}_\omega$ is a single surface enclosing the Γ point, and the total Berry flux is equal to the topological charge at Γ, which is 4. For $\hbar\omega > E_C$ a surface surrounding the *R* point appears such that $\mathbf{S}_\omega$ now encloses two nodes of opposite chirality, driving the net Berry flux, and consequently the CPGE, to zero. The CPGE spectrum calculated from DFT wave functions indeed exhibits an abrupt drop from the $C = 4$ quantization (modified at low energy by spin–orbit interaction) to nearly zero at this energy (**Figure 2*e***; 39).

Finally, a word about corrections to quantization. The expressions leading to CPGE quantization were derived assuming noninteracting Weyl fermions and a two-band Hamiltonian. Corrections arising from non-Weyl bands are proportional to $(\hbar\omega/E_g)^2$ (where E_g is the energy separation of a non-Weyl band) and vanish as optical transitions approach the Weyl points (33). It has been recently pointed out that interactions also lead to corrections to quantization (44) of order $\alpha = e^2/4\pi\epsilon_0\hbar v_F$, which is the fine-structure constant with the group velocity, v_F, replacing the speed of light. This interaction effect is analogous to corrections to quantization in the optical absorption of graphene (45).

4. PHOTOGALVANIC EFFECT EXPERIMENTS

Experimental approaches for measuring PGEs may be categorized by detection techniques. The earliest measurements were conducted using leads deposited directly onto the sample to measure the current generated from a continuous-wave laser source. This approach is required for observing intraband effects driven by THz (terahertz) and mid-IR laser systems, although interband ones can also be observed upon excitation by near-IR and visible sources. Significantly, this technique permits direct measurement of the photogalvanic coefficients provided that the effects of photon drag, lead geometry, and thermally driven currents are properly accounted for.

Noncontact measurements can be performed with the use of short-pulse (i.e., picosecond and femtosecond) laser systems. Here, photogenerated current pulses emit radiation primarily in the 0.1–10-THz frequency range, lending the name THz emission spectroscopy to the technique. The radiation is detected using free-space electro-optic sampling. This technique avoids artifacts from asymmetric electrical contacts and laser-induced heating that must be accounted for in lead-based measurements. Relevant to studies in which crystalline symmetry is important, it also enables continuous and precise determination of the direction of the current through measurement of the polarization of the THz field.

4.1. Experiments on Intraband Photogalvanic Effects

Intraband measurements have been conducted in a broad array of physical systems, including, e.g., topological materials (46) and quantum wells with (47) and without (48) magnetic field, as well as various heterostructures and thin films. Experiments that have focused on the study of spin dynamics (18) and classical (49) and quantum (50) ratchet effects have provided insight on the relative role of heating and inversion symmetry breaking in generating photocurrents in semiconductor

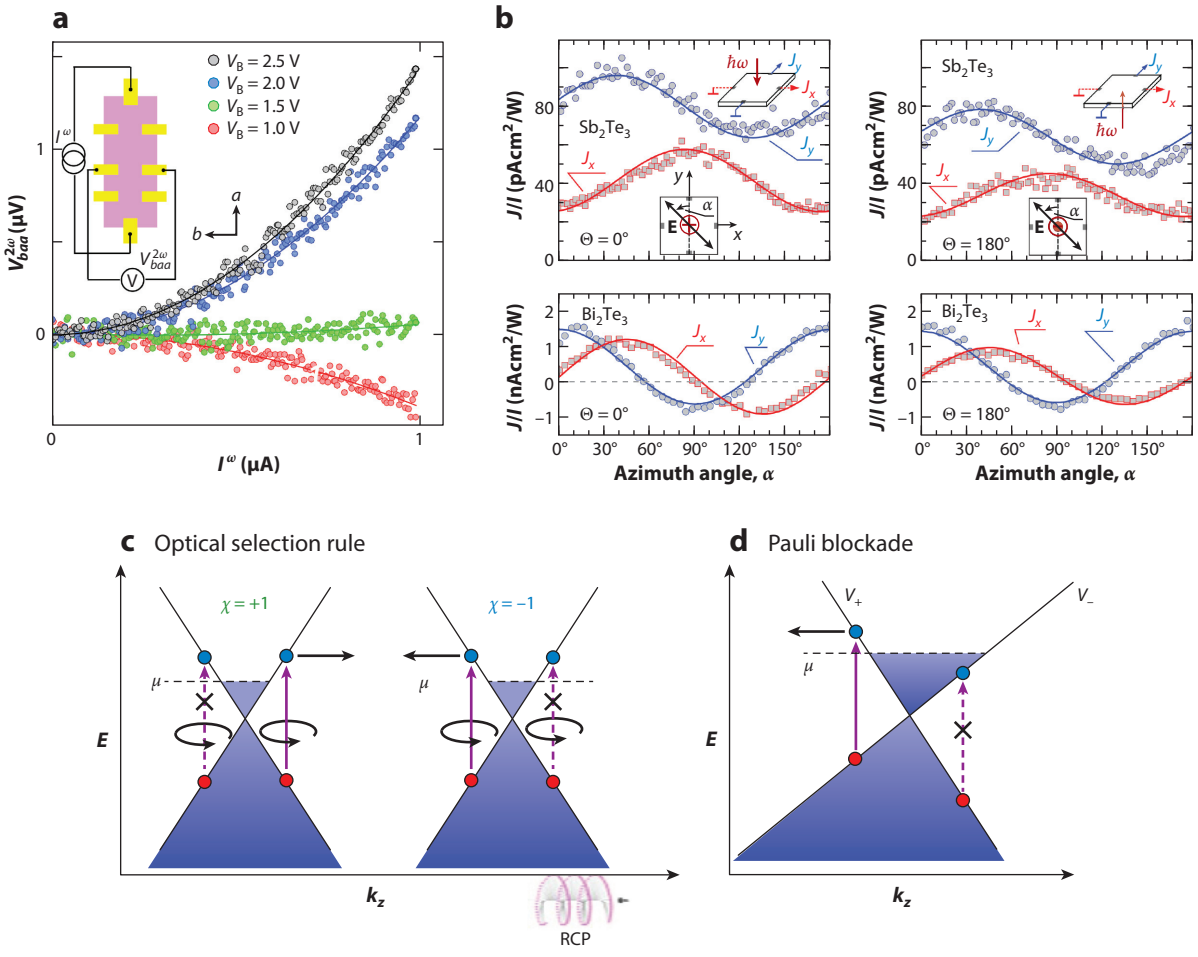

Figure 3

Experimental results on PGEs. (*a*) Quadratic scaling of Hall voltage with longitudinal current. Panel adapted from Reference 52. (*b*) Photocurrent as a function of polarization angle for Bi_2Te_3 and Sb_2Te_3. Left and right subpanels compare photocurrent with light incident from above and below the sample. The absence of a sign flip shows that the current arises from LPGE rather than the photon drag effect. Panel adapted from Reference 53. (*c*) Optical selection rule for untilted and (*d*) tilted Weyl cones. Panel adapted from Reference 54. Abbreviations: LPGE, linear photogalvanic effect; PGE, photogalvanic effect; RCP, right circular polarization.

systems. Intraband PGEs can also be used as probes of the symmetry of optically induced order, as recently demonstrated by Xu et al. (51) in experiments on 1T-$TiSe_2$. Here, cooling through the charge-density wave transition at $T_{CDW} \approx 200$ K in the presence of circularly polarized light was observed to train chiral order, as detected by the onset of a CPGE photoresponse.

In the extreme low-frequency limit, the LPGE is manifest as an NHE (24). Recent experiments on a bilayer sample of the type-II Weyl semimetal WTe_2 reveal the NHE through second harmonics of the driving frequency in tandem with a transverse voltage that scaled quadratically with applied current, as shown in **Figure 3*a*** (52). Through a careful analysis of the effect as a function of applied voltage that tuned interlayer coupling, the authors were able to directly measure the BCD.

PGE studies at THz frequencies on epitaxially grown thin films of the bulk topological insulators Sb_2Te_3 and Bi_2Te_3 revealed the linearly dispersing, spin-momentum-locked surface states that are difficult to separate from the bulk using conventional transport techniques (53). As a second-order optical response forbidden in bulk-centric media, the LPGE uniquely addresses these states because the surface is a locus of inversion symmetry breaking. Experimental evidence that LPGE probes surface transport is seen in **Figure 3*b***, which shows that the dependence of the photocurrent on the direction of the pump field matches the C_{3v} surface point–group symmetry.

4.2. Experiments on Interband Excitation of Weyl Semimetals

Interband effects are accessed through resonant excitation by IR and visible lasers. As with intraband measurements, these experiments can reveal crystal symmetry (52) and spin dynamics (17), and crucially, band structure topology (54). Below, we overview experiments first on mirror symmetric and then chiral systems.

4.2.1. Mirror symmetric Weyls. In the presence of a tilted Weyl dispersion, a circularly polarized excitation field induces an injection current on one side of a Weyl node that is Pauli blocked on the other, as depicted in **Figure 3*c***. The direction, but not the sign, of the induced current is determined by point–group symmetry. However, an analysis of the microscopic mechanism of photocurrent generation revealed that the optical transition matrix elements depend upon the chirality of the node, determining the sign of current flow (38). In experiments that used a CO_2 laser source ($\hbar\omega \sim 100$ meV), Ma and coworkers determined the sign of the topological charge of the W_1 Weyl nodes of TaAs (55). Further studies of the LPGE response in TaAs by Osterhoudt et al. using the same source have shown that TaAs manifests a large second-order conductivity $\sigma_{aac} = 154 \pm 17\ \mu A\ V^{-2}$, highlighting the potential of topological materials for applications in IR sensing (56).

4.2.2. Chiral multifold fermions and the quantized circular photogalvanic effect. As emphasized in Section 3.2, the multifold-fermion system RhSi is an ideal candidate to exhibit a QCPGE. Theoretically, the CPGE takes an especially simple form in the RhSi family of compounds because β_{ij} reduces to a scalar, β, in the cubic space group, $P2_13$ (#198). The THz emission spectrometer, shown schematically in **Figure 4*a***, enables contact-free detection of the LPGE and CPGE currents flowing parallel to the surface of a sample. The inset to **Figure 4*b*** demonstrates direct measurement of CPGE in RhSi (54), as it shows the sign flip of THz transients generated by light of opposite helicity. The transients are time-resolution limited, indicating that even subpicosecond photoexcitation yields a quasi–steady state in which the photocurrent is proportional to the product of β and the momentum relaxation time, τ. **Figure 4*b*** shows the CPGE amplitude (proportional to $\beta\tau$) in RhSi as a function of $\hbar\omega$ in the range from 0.5 to 1.1 eV. The striking feature of the spectrum is the rapid drop in amplitude that occurs when $\hbar\omega$ exceeds 0.65 eV. Above this energy, $\beta\tau$ decays from its peak value by a factor of ~200 as $\hbar\omega$ reaches 1.1 eV. The photon energy at which the CPGE response decreases agrees remarkably well with the theoretical prediction (36) previously shown in **Figure 2*e***.

5. OPTICAL SECOND-HARMONIC GENERATION IN NONCENTROSYMMETRIC METALS

Although the magnitude of nonlinear optical responses such as the PGE and, to a limited extent, SHG (57, 58) encode information about the band topology of a material, the structure of nonlinear

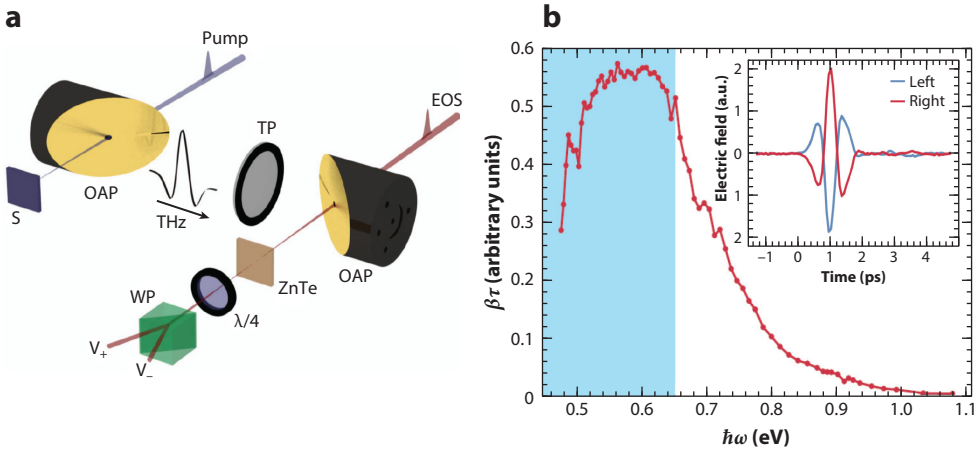

Figure 4

(*a*) Terahertz emission spectrometer for measurement of CPGE in RhSi. The component of photogalvanic current parallel to the surface of the RhSi crystal radiates a THz pulse that is collected, collimated, and focused onto a ZnTe crystal for time-resolved electro-optic sampling of the THz transient. (*b*) CPGE spectrum of RhSi as a function of pump photon energy. Adapted from Reference 54. Abbreviations: CPGE, circular photogalvanic effect; EOS, electro-optic sampling; OAP, off-axis paraboloid; S, sample; THz, terahertz; TP, terahertz polarizer; WP, Wollaston prism.

optical susceptibility tensors encodes detailed symmetry information about a material owing to their high rank. Measuring the tensor structure is therefore a highly sensitive means of refining the crystallographic, electronic, and magnetic point–group symmetries of a solid. As discussed in a number of reviews (59–62), this technique can be applied to study surfaces, buried interfaces, and nanoscale devices, which are typically challenging for diffraction-based probes. The technique is also increasingly being used to search for exotic order parameters, which are manifested through subtle changes in point–group symmetries across a phase transition. In this section, we present an overview of the technique in the context of SHG, followed by a selection of illustrative recent experiments revealing spontaneous inversion symmetry breaking in metals.

5.1. Symmetry Refinement from Second-Harmonic Generation

The nonlinear optical susceptibility tensor is a central concept for the symmetry refinement of a material via SHG. In this section, we describe the mathematical structure of the tensor, how it arises from several different electromagnetic response channels, and how its structure can be used to determine material point–group symmetries.

5.1.1. Second-harmonic optical responses. A material illuminated by an electromagnetic wave may respond in several ways, including in general through an induced electric polarization, P_i; magnetization, M_i; and electric quadrupole density, Q_{ij}. Each of these response channels will subsequently act as a source for outgoing radiation via the associated induced current density, J_i (63):

$$J_i = \frac{\partial P_i}{\partial t} + \varepsilon_{ijk}\nabla_j M_k - \nabla_j \frac{\partial Q_{ij}}{\partial t}, \qquad 20.$$

where ε_{ijk} is the Levi–Civita symbol, and summation over repeated indices is implied. In the frequency domain, each material response can be expanded as a series in the applied electric (E_i) and

magnetic (H_i) fields and their gradients (59):

$$P_i = \chi_{ij}^{\mathrm{ee}} E_j + \chi_{ij}^{\mathrm{em}} H_j + \chi_{ijk}^{\mathrm{eq}} \nabla_j E_k + \chi_{ijk}^{\mathrm{eee}} E_j E_k + \chi_{ijk}^{\mathrm{eem}} E_j H_k + \chi_{ijkl}^{\mathrm{eeq}} E_j \nabla_k E_l + \cdots \quad 21.$$

$$M_i = \chi_{ij}^{\mathrm{me}} E_j + \chi_{ij}^{\mathrm{mm}} H_j + \chi_{ijk}^{\mathrm{mq}} \nabla_j E_k + \chi_{ijk}^{\mathrm{mee}} E_j E_k + \chi_{ijk}^{\mathrm{mem}} E_j H_k + \chi_{ijkl}^{\mathrm{meq}} E_j \nabla_k E_l + \cdots \quad 22.$$

$$Q_{ij} = \chi_{ijk}^{\mathrm{qe}} E_k + \chi_{ijk}^{\mathrm{qm}} H_k + \chi_{ijkl}^{\mathrm{qq}} \nabla_k E_l + \chi_{ijkl}^{\mathrm{qee}} E_k E_l + \chi_{ijkl}^{\mathrm{qem}} E_k H_l + \chi_{ijklm}^{\mathrm{qeq}} E_k \nabla_l E_m + \cdots \quad 23.$$

Here, the χ expansion coefficients are the various optical susceptibility tensors of the material. The first letter in the superscript of a susceptibility represents the type of material response it encodes [e for electric dipole (ED), m for magnetic dipole (MD), and q for electric quadrupole (EQ)], whereas the remaining letters represent the types of field perturbations inducing the response. Terms containing only one power of a field express the familiar linear electromagnetic response of a material. For example, χ^{ee} and χ^{mm} encode the dielectric function, $\epsilon = \epsilon_0 + \chi^{\mathrm{ee}}$, and magnetic permeability, $\mu = \mu_0(1 + \chi^{\mathrm{mm}})$, respectively, and χ^{em} and χ^{me} describe the linear magnetoelectric effect. Terms containing more than one power of the fields represent the nonlinear optical response. (See the sidebar titled Quantum Mechanical Expressions.)

Series expansions of this sort, along with the multitude of possible response channels, lead to a proliferation of expressions. Many ostensibly disparate terms, however, can be unified (65). For example, an electromagnetic plane wave oscillating at frequency ω has $\nabla \times \mathbf{E} = i\omega\mu\mathbf{H}$. Thus, the MD response, $P_i = \chi_{ijk}^{\mathrm{eem}} E_j H_k$, can be rewritten in the form of an EQ response: $P_i = (\chi_{ijk}^{\mathrm{eem}} \mu_{kl}^{-1} \varepsilon_{lmn}/i\omega) E_j \nabla_m E_n$. In other words, the third-rank mixed polar–axial pseudotensor $\chi_{ijk}^{\mathrm{eem}}$ can be converted into a fourth-rank pure polar tensor $\chi_{ijmn} = \chi_{ijk}^{\mathrm{eem}} \mu_{kl}^{-1} \varepsilon_{lmn}/i\omega$. This highlights the fact that EQ and MD transitions occur at the same order, being the symmetric and antisymmetric parts of the same electromagnetic perturbation. With conversions like these and Equation 20, the numerous terms from the various source and response channels can be consolidated. In this section, we focus on SHG, and neglecting all terms except those containing two

QUANTUM MECHANICAL EXPRESSIONS

The optical response of a material can be described in the language of photons: The material absorbs one or more photons (for linear and nonlinear responses, respectively) from the incident electromagnetic wave and emits a single photon to the outgoing wave. Within this picture, perturbation theory can be used to derive expressions for the various optical susceptibility tensors (64). For example, keeping only resonant terms, one obtains

$$\chi_{ij}^{\mathrm{ee}}(\omega) = \frac{N}{\hbar} \sum_n \frac{\langle \psi_g | p_i | \psi_n \rangle \langle \psi_n | p_j | \psi_g \rangle}{\omega_{ng} - \omega},$$

$$\chi_{ijk}^{\mathrm{eem}}(2\omega) = \frac{\mu_0 N}{\hbar^2} \sum_{n,n'} \frac{\langle \psi_g | p_i | \psi_{n'} \rangle \langle \psi_{n'} | p_j | \psi_n \rangle \langle \psi_n | \mu_k | \psi_g \rangle}{(\omega_{n'g} - 2\omega)(\omega_{ng} - \omega)} + (n \leftrightarrow n'),$$

where N is the number density of electrons, p (μ) is the electric (magnetic) dipole operator, n and n' label excited states above the ground state g, ω is the incident light frequency, and $\hbar\omega_{ab} = E_a - E_b$ is the energy difference between two levels. With these equations, the meaning of the superscripts on the susceptibility tensors is made clear: They indicate the types of electronic transitions involved in the particular response channel, each of which is associated with a perturbation operator matrix element in the numerator. Resonance conditions—matching incoming and outgoing photon energies to the corresponding difference in energy levels participating in the transition—are often utilized to enhance SHG yield.

powers of the electromagnetic field, one obtains the central equation,

$$J_i^{(2)}(2\omega) = \chi_{ijk}^{(2)} E_j(\omega) E_k(\omega) + \chi_{ijkl}^{(2)} E_j(\omega) \nabla_k E_l(\omega) + \mathcal{O}\left(\nabla^2 E\right), \quad 24.$$

where, in terms of the above susceptibility tensors,

$$\chi_{ijk}^{(2)} = -2i\omega \chi_{ijk}^{\mathrm{eee}}, \quad 25.$$

$$\chi_{ijkl}^{(2)} = 2\varepsilon_{ikm} \chi_{mjl}^{\mathrm{mee}} + 4i\omega \chi_{ikjl}^{\mathrm{qee}} - 2i\omega \chi_{ijkl}^{\mathrm{eeq}} - 2\chi_{ijm}^{\mathrm{eem}} \mu_{mn}^{-1} \varepsilon_{nkl}. \quad 26.$$

The first term, proportional to a third-rank tensor, represents leading-order ED SHG. The second term, proportional to a fourth-rank tensor, represents combined MD and EQ SHG. For magnetically ordered media, these SHG tensors can be further classified depending on whether they are time-reversal even (*i* type) or odd (*c* type). As has been extensively reviewed in References 59, 66, and 67, this makes SHG a sensitive probe of magnetic point–group symmetries and magnetic domains in bulk crystals and nanoscale devices and at surfaces and interfaces.

5.1.2. Symmetry refinement procedure. The structure of a nonlinear optical susceptibility tensor can be determined through rotational anisotropy experiments, whereby the nonlinear optical response is measured as a function of the light polarization, scattering plane angle, and angle of incidence (61). From these measurements, the nonzero and independent elements of the tensor can be extracted in a straightforward way and compared with expectations from candidate point groups. Recent technical advancements have made rotational anisotropy data collection precise and rapid (68, 69).

Key to detecting symmetry-breaking orders is Neumann's principle, which states that a property tensor must respect all of the physical symmetries of a material. More explicitly, a particular coordinate transformation that leaves a crystal invariant must also leave the susceptibility tensor invariant. For example, if T_{ij} is a coordinate transformation matrix corresponding to some point–group symmetry of the material, then for a polar tensor,

$$\chi_{ijk\cdots} = T_{ip} T_{jq} T_{kr} \cdots \chi_{pqr\cdots}. \quad 27.$$

This imposes significant constraints on the tensor structure, dictating which tensor elements are allowed to be nonzero and independent. As a particularly important example, if the material possesses inversion symmetry ($T_{ij} = -\delta_{ij}$), then odd-rank polar tensors must vanish because $\chi_{ijk\cdots} = -\chi_{ijk\cdots}$. This leads to the well-known result that leading-order ED SHG can only occur in the bulk of noncentrosymmetric materials. Higher-order processes governed by odd-rank axial tensors or even-rank polar tensors, such as MD and EQ responses, respectively, as well as ED responses from surfaces and interfaces (where inversion symmetry is necessarily lost), are nonetheless allowed in centrosymmetric materials. These processes, however, are generally much weaker than the bulk ED response (59, 64). For this reason, SHG is ideally suited to detecting spontaneously broken inversion symmetry, where the leading-order bulk ED susceptibility $\chi_{ijk}^{\mathrm{eee}}$ becomes nonzero at the phase transition and encodes information about the symmetries and magnitude of the order parameter. In the next section, we present several illustrative examples of spontaneous inversion symmetry-broken metals uncovered in this way. (See the sidebar titled Landau Theory in Nonlinear Optics.)

5.2. Application to Polar and Piezoelectric Metals

Metals cannot sustain an internal electric field, and the long-range Coulomb interaction that stabilizes ferroelectricity in dielectrics is effectively screened by mobile charge carriers in conducting

LANDAU THEORY IN NONLINEAR OPTICS

Landau theory is the theoretical framework through which spontaneous symmetry breaking at phase transitions may be understood. Within the theory, the free energy of a material is expanded as a Maclaurin series in the relevant order parameters of the system. Each order parameter transforms according to an irreducible representation of the symmetry group of the system, and each polynomial term allowed in the series must be invariant under every element of the symmetry group. By including electric (polar vector representation) and magnetic (axial vector representation) fields as external order parameters in addition to the internal order parameters of the material, one may calculate various optical susceptibility tensors (70). For example, a hypothetical free-energy expansion respecting inversion symmetry is

$$F = F_0 + \frac{a}{2}P^2 - \mathbf{E}\cdot\mathbf{P} - b\phi_u P_x(E_y^2 - E_z^2) + \cdots,$$

where $\mathbf{E}$ and $\mathbf{P}$ are the external electric field and internal electric polarization, respectively; ϕ_u represents an odd-parity multipolar order parameter that condenses at some critical point due to terms in the free energy not shown; and a and b are series expansion coefficients. The $\mathbf{E}\cdot\mathbf{P}$ term enters the free energy because the external electric field is conjugate to the internal electric polarization. We emphasize here that symmetry alone dictates the form of the term that couples ϕ_u to $\mathbf{E}$ and $\mathbf{P}$. By minimizing the free energy with respect to P_x ($\partial F/\partial P_x = 0$), one obtains $P_x = E_x/a + b\phi_u(E_y^2 - E_z^2)/a + \cdots$, from which the linear and nonlinear optical susceptibilities, $\chi_{xx}^{ee} = 1/a$ and $\chi_{xyy}^{eee} = -\chi_{xzz}^{eee} = b\phi_u/a$, may be easily extracted. The nonlinear susceptibility is directly proportional to the odd-parity order parameter, ϕ_u, making it an experimental handle for both the magnitude and symmetries of that order. Automated tools exist for computing all of the allowed invariant polynomials of a crystal (see, for example, Reference 71).

systems. Nevertheless, in 1965, Anderson & Blount proposed that ferroelectric-like structural phase transitions can occur in what are now known as polar metals (9). They argued that although free electrons completely screen the average internal electric field in a metal, they do not suppress transverse optical phonons and Lorentz local fields, which can support internal symmetry changes similar to those occurring in conventional ferroelectrics. The modern consensus is that metallic conduction and polar distortions are not fundamentally incompatible (12). More general considerations apply to the broader class of rare piezoelectric metals, which break inversion symmetry but do not necessarily have a unique polar axis. Metals can host a number of competing electronic orders, such as charge density waves or superconductivity, and the interplay between these Fermi liquid instabilities and inversion symmetry breaking is an active area of research.

Measuring the order parameter of a polar metal presents a unique challenge. The conventional method to quantify the polarization P of a sample is via electrical means: measuring the transfer of charge across a sample after reversing an applied voltage. Using a parallel plate capacitor geometry, P can be inferred using the relations $P = Q/2A$ and $Q = \int I(t)\mathrm{d}t$, where $I(t)$ is the measured current flowing from one plate to the other, Q is the total charge transferred, and A is the plate area. The factor of 2 arises from the reversal of the polarization direction in the sample. This procedure is deeply rooted in the "modern theory of polarization," which informs that only changes in electric polarization are physically measurable (72, 73). This method fails for conducting systems because the sample will electrically short the capacitor plates. It also fails for nonpolar piezoelectric metals, where no macroscopic transfer of charge occurs in the material. By contrast, optical SHG is an ideal experimental technique for measuring the magnitude of an odd-parity order parameter—regardless of sample conductivity—through its proportionality with the nonlinear optical susceptibility, χ_{ijk}^{eee}. SHG has long been a standard tool for probing insulating

ferroelectrics (60), and below we present three exemplary piezoelectric or polar metals recently investigated with the technique.

5.2.1. Multipolar electronic nematic order in $Cd_2Re_2O_7$. In recent years, nonlinear optics has emerged as a powerful technique to uncover so-called hidden orders, defined as equilibrium phases of matter that are invisible to conventional experimental probes (62). One common class of examples is multipolar order that does not directly couple to any conjugate external field. The nonlinear optical susceptibility tensor $\chi^{(2)}$, however, encodes the total lattice, electronic, and magnetic point–group symmetries of a material and is sensitive to such order.

The superconducting pyrochlore, $Cd_2Re_2O_7$, is a strongly spin–orbit coupled metal with an unusual inversion symmetry-breaking phase transition at 200 K. Early nonlinear optical experiments discovered a tensor order parameter with E_u symmetry associated with the freezing of a soft phonon mode at the phase transition, consistent with a Landau theory analysis of phonon instabilities (74, 75). Other experimental evidence, however, called into question the importance of lattice degrees of freedom in the origin of the phase transition. In particular, though structural changes at the phase transition are unusually small (atomic displacements less than ~0.01 Å), dramatic changes in electronic properties such as electrical resistivity and magnetic susceptibility are observed (76–79). Further puzzling is the absence of any magnetic or charge order in the material (80).

Inspired by the theoretical prediction of novel parity-breaking Fermi liquid instabilities in correlated spin–orbit coupled metals (81), Harter et al. used SHG to reexamine the odd-parity order parameters involved in the 200-K phase transition in $Cd_2Re_2O_7$ (82). Consistent with previous studies, they detected a dominant structural order parameter with E_u symmetry, but found an unexpected linear temperature dependence ($\propto 1 - T/T_c$) inconsistent with a primary order parameter driving the phase transition. Instead, they discovered an additional order parameter with T_{2u} symmetry and mean-field-like temperature dependence ($\propto\sqrt{1 - T/T_c}$) matching the prior theoretical prediction of possible multipolar nematic Fermi liquid instabilities in spin–orbit coupled metals (81). They concluded that the T_{2u} order parameter was electronic in origin and drove the phase transition, with the E_u structural order parameter of a secondary nature, pulled along by a coupling term in the Landau free energy. Their symmetry analysis necessitated the existence of an additional primary order parameter with T_{1g} even-parity symmetry. The resulting free energy took the form $F = F_0 + (T/T_c - 1)(a_u\phi_u^2 + a_g\phi_g^2) + b\psi^2 + c\phi_u\phi_g\psi + \cdots$, with ϕ_u and ϕ_g the T_{2u} and T_{1g} primary orders, respectively, and ψ the E_u secondary structural order. A summary of the experimental steps taken by Harter et al. is shown in **Figure 5**. This unusual phase transition was verified in a subsequent study, which used ultrafast coherent phonon spectroscopy and time-resolved SHG to study the dynamics of the E_u structural distortion (83). An explanation for the Landau-violating nature of the phase transition in $Cd_2Re_2O_7$ is still an open question, but the phenomenology is remarkably similar to so-called improper ferroelectrics (84, 85). Magnetic scenarios have been put forth to explain the observations (86), but there remains no evidence for magnetic order in the material.

5.2.2. Polar metallicity in $LiOsO_3$. In 2013, $LiOsO_3$ became the first metallic system conclusively determined to undergo a continuous phase transition associated with the formation of a polar axis (87). Upon cooling below 140 K, the crystal symmetry of $LiOsO_3$ lowers from $R\bar{3}c$ to $R3c$ as the Li^+ ions collectively shift off center along the cubic [111] direction. This behavior is structurally identical to the ferroelectric transition in insulating $LiNbO_3$. After this initial discovery, Padmanabhan et al. employed SHG to better understand the role of metallicity in the polar phase transition (88). They found that the magnitude of the nonlinear susceptibility

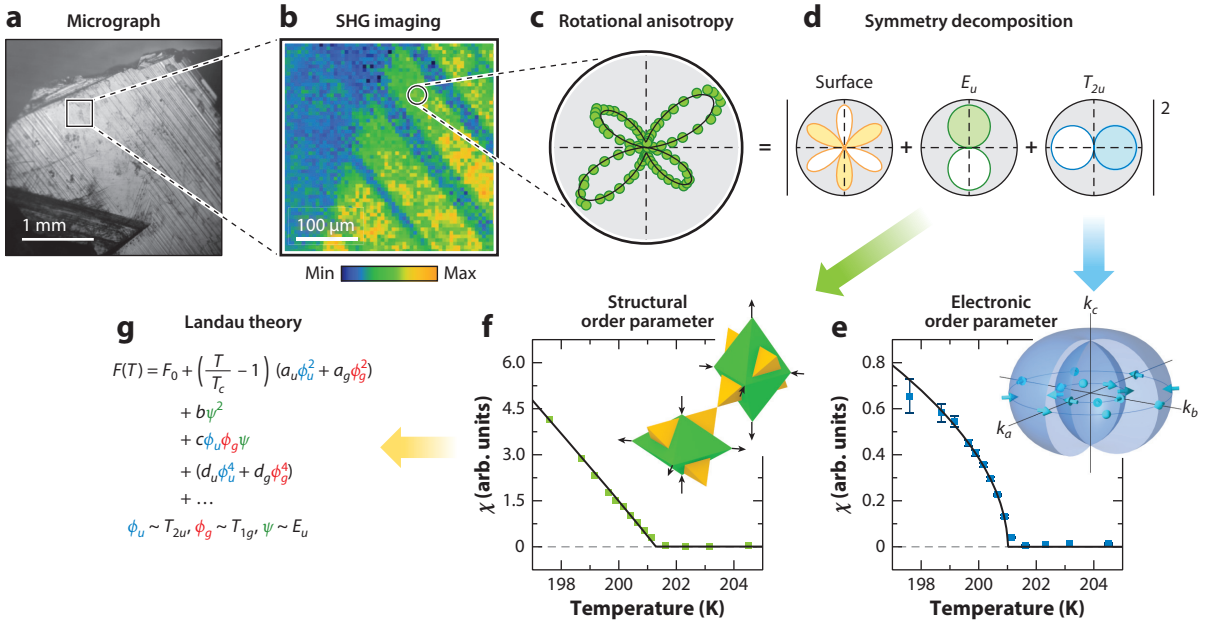

Figure 5

Steps used to uncover multipolar electronic nematic order in $Cd_2Re_2O_7$ with optical SHG. (*a*) At a pristine area of the sample surface, low-temperature SHG microscopy is used to identify large domains. (*b*) SHG rotational anisotropy patterns are then collected within a single domain. (*c*) The patterns are decomposed into orthogonal symmetry channels, and (*d*) the amplitude of each irreducible representation is extracted for a series of sample temperatures to produce (*e*,*f*) order parameter temperature dependence curves. The temperature dependence is then fed into (*g*) a Landau free-energy model for the material, which subsequently sheds light on the physical nature of the orders. Figure adapted from Reference 82. Abbreviation: SHG, second-harmonic generation.

in the polar direction was significantly weaker in $LiOsO_3$ than in the isostructural insulating ferroelectrics $LiNbO_3$ and $LiTaO_3$. This effect likely arises from the substantially smaller Os–O acentric displacements in $LiOsO_3$ due to the weak coupling mechanism that stabilizes the polar metallic phase (10), a picture confirmed by recent time-resolved optical experiments (89). Temperature-dependent SHG experiments, together with complementary Raman spectroscopy measurements of phonon mode lifetimes, showed that the polar phase transition in $LiOsO_3$ is continuous and likely of an order–disorder nature. The Landau free energy at the phase transition has the classic form $F = F_0 + a(T/T_c - 1)p^2 + bp^4 + \cdots$, where p is an order parameter transforming like the A_{2u} irreducible representation of the $\bar{3}m$ point group, corresponding to a polarization along the cubic [111] direction. Aided by SHG microscopy, Padmanabhan et al. uncovered 109° and 71° ferroelastic domain walls associated with the breaking of C_4 symmetry. No 180° polar domain walls were observed, however, which is consistent with the screening by free electrons of depolarizing fields that otherwise prevent the formation of large single domains in conventional ferroelectrics. After the initial discovery of polar metallicity in $LiOsO_3$, other polar metals have been investigated with SHG microscopy. The layered Ruddlesden–Popper material, $Ca_3Ru_2O_7$, for example, hosts a rich polar domain structure at room temperature (90).

5.2.3. Ferroelectric enhancement of superconductivity in strained $SrTiO_3$. The perovskite titanates have proven fruitful for creating polar metals. For example, a polar metallic phase emerges upon electron doping of the canonical ferroelectric $BaTiO_3$ (91), and

$BaTiO_3/SrTiO_3/LaTiO_3$ thin film heterostructures host quasi-two-dimensional polar metallic interfacial states (92). Bulk-insulating $SrTiO_3$ is known as a quantum paraelectric because an incipient polar instability is avoided at low temperatures by quantum fluctuations of the material's ground state. In thin films, however, ferroelectricity can be stabilized through both tensile and compressive epitaxial strain, giving rise to in-plane and out-of-plane polarization vectors, respectively (93–95). Indeed, temperature-dependent SHG measurements confirm that a ferroelectric phase transition occurs in compressively strained stoichiometric $SrTiO_3$ films (96, 97). When lightly doped, $SrTiO_3$ becomes metallic and superconducts at low temperatures despite relatively dilute carrier densities ($\sim 10^{20}$ cm^{-3}). Furthermore, the superconducting critical temperature can be enhanced by up to a factor of two through compressive strain (98). In this doping regime, the Debye frequency exceeds the Fermi energy, invalidating the conventional Bardeen–Cooper–Schrieffer theory of superconductivity and demanding a different, as-yet-unknown, Cooper pairing mechanism.

To study the link between enhanced superconductivity and ferroelectricity in compressively strained $SrTiO_3$ films, Russell et al. used SHG to measure the doping and temperature dependence of the ferroelectric-like order parameter (99). They found that the doping-dependent onset of spontaneous polarization correlated perfectly with upturns in electrical resistivity. Such behavior likely results from screening of polar charges, which causes carriers to localize at the film surface and depletes them from the bulk. By developing a long-range mean-field Ising model of the order parameter, they were able to quantitatively fit the temperature dependence of the SHG intensity. The Landau free energy of their model takes the form $F = F_0 + a(T/T_c - 1)p^2 + bp^4 - Ep + \cdots$, which is identical to the $LiOsO_3$ free energy but with the additional term $-Ep$, corresponding to a weak extrinsic polarizing field E breaking the intrinsic $\pm p$ symmetry of the polarization. This field is due to the dissimilar vacuum and substrate interfaces sandwiching the film. The success of their model—in particular, the quantitative agreement with an Ising-like polarization—strongly supports the notion that the ferroelectric phase transition in compressively strained $SrTiO_3$ is of an order–disorder nature, as in $LiOsO_3$. This, together with the observation of enhanced superconductivity deep within the polar phase, places significant constraints on possible mechanisms of superconductivity in $SrTiO_3$, such as soft mode fluctuations.

5.2.4. Effect of short-range correlations on second-harmonic generation. The previous examples illustrate how the emergence of a local parameter is manifested in SHG via the appearance of a new radiation process that becomes allowed upon symmetry lowering. Recently, however, it has been shown that critical fluctuations preceding a phase transition can also be detected by SHG. Because no symmetry reduction has yet occurred in this state, no new SHG radiation processes or susceptibility tensor elements emerge. Rather, the fluctuations are manifested through changes in the already existing symmetry-allowed tensor elements. To understand how such changes arise, consider for simplicity local dipolar degrees of freedom S_i in a crystal, which could represent electric or magnetic dipoles, interacting via a nearest-neighbor Ising-type Hamiltonian $\mathcal{H}_{\text{int}} = \sum_{\langle ij \rangle} J_{ij} S_i S_j$. In general, the coupling constants J_{ij} depend sensitively on the position of atoms in the vicinity of sites i and j that mediate the interaction. In polar metals, for example, short-range dipolar interactions are driven by the local bonding environment of cations in the unit cell, making it sensitive to anion positioning. In magnetic insulators, superexchange interactions are similarly sensitive to cation–anion–cation bond angles. The atomic positions minimize the total energy of the system $E_T = \langle \mathcal{H}_{\text{int}} \rangle + \langle \mathcal{H}' \rangle$, where $\mathcal{H}'$ includes all other interactions and the angular brackets denote thermal expectation values. As the system approaches the phase boundary from the disordered side, the dipole correlator $\langle S_i S_j \rangle$, and thus $\langle \mathcal{H}_{\text{int}} \rangle$, increases while the order parameter $\langle S_i \rangle$ remains zero. In turn, atomic positions will shift to readjust the balance between

$\langle \mathcal{H}_{\text{int}} \rangle$ and $\langle \mathcal{H}' \rangle$ in order to minimize E_T, which then alters the relative magnitudes of the existing SHG tensor elements.

Ron et al. first demonstrated this approach on the layered ferromagnetic insulator $CrSiTe_3$ using high-sensitivity SHG rotational anisotropy measurements (100). They showed that the growth of the intralayer and interlayer spin correlators ($\langle S_i S_j \rangle_{\parallel}$ and $\langle S_i S_j \rangle_{\perp}$) is accompanied by atomic displacements along two different normal coordinates of the lattice that preserve overall symmetry, which act to enhance the intralayer and interlayer superexchange and thereby increase $\langle \mathcal{H}_{\text{int}} \rangle$. Because these two types of distortion couple to distinct subsets of χ^{qee}_{ijkl} elements allowed under the centrosymmetric point group of $CrSiTe_3$, Ron et al. were able to independently track the temperature dependence of $\langle S_i S_j \rangle_{\parallel}$ and $\langle S_i S_j \rangle_{\perp}$ by measuring changes in different subsets of χ^{qee}_{ijkl} elements above the Curie temperature.

More recently, similar effects were also reported in $LiOsO_3$ above its polar transition temperature ($T_c = 140$ K) (101). As discussed previously, all χ^{eee}_{ijk} tensor elements couple linearly to the polar order parameter and dominate the SHG response below T_c. However, there exists an additional weaker EQ SHG response that is allowed even above T_c in the centrosymmetric phase, whose magnitude varies as a function of the angle of incidence approximately like $\sin^2\theta$. Therefore this contribution is nearly undetectable under normal incidence conditions (88), but can be amplified by increasing θ. As shown in **Figure 6**, the EQ SHG response from $LiOsO_3$ measured with obliquely incident light starts to grow below around 230 K, in clear contrast to the normal incidence data. The shapes of SHG rotational anisotropy patterns also change drastically between 230 K and T_c, signifying nonuniform changes in the χ^{qee}_{ijkl} elements taking place over this temperature window. Such changes were attributed to symmetry preserving structural distortions that occur in response to the growth of the electric dipole correlator, analogous to the situation in $CrSiTe_3$. Note that changes in the χ^{eee}_{ijk} tensor must be uniform because all elements are proportional to the order parameter, which fixes the shape of the rotational anisotropy patterns below T_c.

Simplified hyperpolarizable bond models (102, 103), which assume that SHG radiation arises from the classical anharmonic motion of charges along different chemical bond directions, have been successfully used to establish qualitative connections between specific structural distortions and changes in specific χ^{eee}_{ijk} tensor elements. But more sophisticated models will be needed to draw quantitative information about distortion amplitudes from SHG intensity changes. Nonetheless, this technique extends the application of SHG to the study of short-range correlations in addition to symmetry-breaking phase transitions. It also highlights the importance of distinguishing between multiple sources of SHG intensity change that can occur in quantum materials.

6. FUTURE DIRECTIONS

Progress in the detection and interpretation of nonlinear optical responses is creating new opportunities for revealing the topological structure of condensed matter systems. We cannot hope to anticipate the most impactful directions, as it is notoriously difficult to make predictions, especially about the future. However, we anticipate that advances in SHG spectroscopy will continue to improve our understanding of how materials that potentially support topological band structures are stabilized and how they can be identified and manipulated. Another path that is particularly promising exploits the natural synergy among PGEs, SHG, and optical microscopy in both near- and far-field versions. Here, one measures the PGE current and/or second-harmonic emission generated by a metallic tip or laser focal spot that scans across a sample. The resulting image will report locations with local inversion breaking, in principle with nanometer resolution.

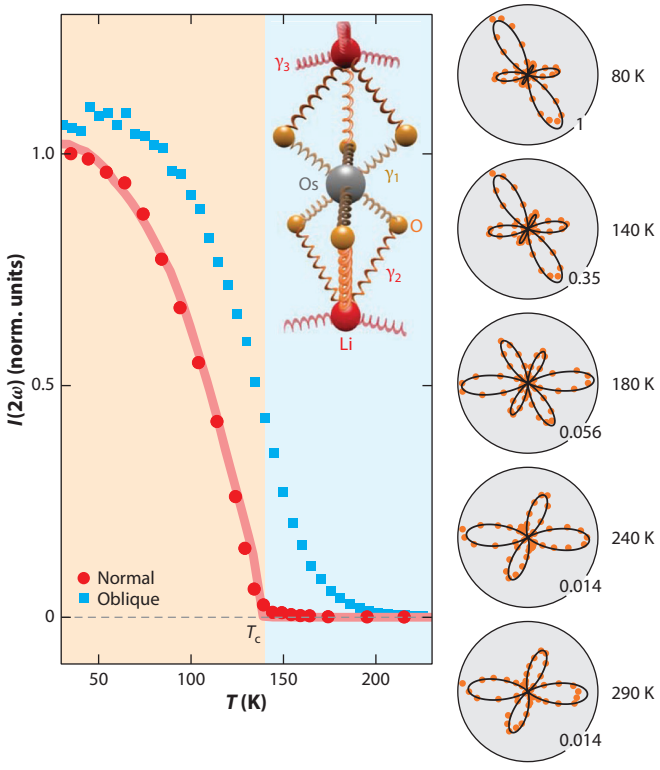

Figure 6

SHG intensity from a [121]-oriented $LiOsO_3$ crystal measured under normal and oblique incidence geometries. The latter is sensitive to the electric quadrupole SHG contribution, which measures short-range dipolar-correlation-induced structural distortions that onset well above $T_c = 140$ K. SHG rotational anisotropy patterns at select temperatures (*right*) show that nonuniform changes occur in the range of $T_c < T < 230$ K, where short-range correlations develop. These shape changes can be captured via the simplified hyperpolarizable bond model illustrated in the inset. By changing the hyperpolarizability of the bonds ($\gamma_1, \gamma_2, \gamma_3$), the data are well reproduced by the model (*black lines*). Figure adapted from Reference 101. Abbreviation: SHG, second-harmonic generation.

Once identified, local spectroscopy of such regions becomes possible, with the potential to reveal topologically protected and correlated states at domain boundaries where inversion breaking occurs naturally. Another promising avenue is to explore changes in topology across spontaneous inversion-breaking transitions in metals using PGEs and SHG, with an eye toward controlling topological responses on demand. We hope that the promise of the PGE and SHG techniques will drive future experimental innovation as well as theoretical research to understand the nonlinear optical response of inversion-breaking superconductors (104) and other correlated phases, particularly in low-dimensional and interfacial structures.

DISCLOSURE STATEMENT

The authors are not aware of any affiliations, memberships, funding, or financial holdings that might be perceived as affecting the objectivity of this review.

ACKNOWLEDGMENTS

T.M. was supported by Japan Science and Technology Agency (JST) PRESTO (Precursory Research for Embryonic Science and Technology; JPMJPR19L9), and JST CREST (Core Research for Evolutional Science and Technology; JPMJCR19T3). D.H. acknowledges funding from the Army Research Office (W911NF-16-1-0361, W911NF-17-1-0204), the Department of Energy (DOE; DE SC0010533), the National Science Foundation(NSF; PHY-1733907), and the David and Lucile Packard Foundation. J.O. and J.E.M. acknowledge funding from the Quantum Materials program at Lawrence Berkeley National Laboratory, supported by the Office of Basic Energy Sciences, Materials Sciences and Engineering Division of the U.S. DOE under contract no. DE-AC02-05CH11231. J.E.M. acknowledges support from a Simons Investigatorship, and J.O. acknowledges support from the Gordon and Betty Moore Foundation's EPiQs (Emergent Phenomena in Quantum Systems) Initiative through grant no. GBMF4537. J.W.H. acknowledges support from the Materials Research Science and Engineering Centers (MRSEC) program of the NSF under grant number DMR-1720256 (Seed Program) and the UCSB NSF Quantum Foundry through Q-AMASE-i program award number DMR-1906325.

LITERATURE CITED

1. Bradlyn B, Elcoro L, Cano J, Vergniory MG, Wang Z, et al. 2017. *Nature* 547:298–305
2. Xu SY, Belopolski I, Alidoust N, Neupane M, Bian G, et al. 2015. *Science* 349:613–17
3. Lv B, Weng H, Fu B, Wang X, Miao H, et al. 2015. *Phys. Rev. X* 5:031013
4. Yang LX, Liu ZK, Sun Y, Peng H, Yang HF, et al. 2015. *Nat. Phys.* 11:728–32
5. Belinicher VI, Sturman BI. 1980. *Sov. Phys. Usp.* 23:199
6. Sturman BI, Fridkin VM. 1992. *Photovoltaic and Photorefractive Effects in Noncentrosymmetric Materials*. Boca Raton, FL: CRC
7. Nagaosa N, Sinova J, Onoda S, MacDonald AH, Ong NP. 2010. *Rev. Mod. Phys.* 82:1539–92
8. Boyd RW. 2003. *Nonlinear Optics*. London: Academic
9. Anderson PW, Blount EI. 1965. *Phys. Rev. Lett.* 14:217–19
10. Puggioni D, Rondinelli JM. 2014. *Nat. Commun.* 5:3432
11. Kim TH, Puggioni D, Yuan Y, Xie L, Zhou H, et al. 2016. *Nature* 533:68–72
12. Benedek NA, Birol T. 2016. *J. Mater. Chem. C* 4:4000–15
13. Van der Ziel J, Pershan PS, Malmstrom L. 1965. *Phys. Rev. Lett.* 15:190
14. Belinicher V, Ivchenko E, Sturman B. 1982. *Zh. Eksp. Teor. Fiz.* 83:649–61
15. Fregoso BM, Morimoto T, Moore JE. 2017. *Phys. Rev. B* 96:075421
16. Asnin VM, Bakun AA, Danishevskii AM, Ivchenko EL, Pikus GE, Rogachev AA. 1979. *Solid State Commun.* 30:565–70
17. Ganichev SD, Prettl W. 2003. *J. Phys.: Condens. Matter* 15:R935–83
18. Ganichev S, Danilov S, Bel'kov V, Giglberger S, Tarasenko S, et al. 2007. *Phys. Rev. B* 75:155317
19. Chang MC, Niu Q. 1995. *Phys. Rev. Lett.* 75:1348–51
20. Resta R. 1994. *Rev. Mod. Phys.* 66:899–915
21. Xiao D, Chang MC, Niu Q. 2010. *Rev. Mod. Phys.* 82:1959–2007
22. Chong YD. 2010. *Phys. Rev. B* 81:052303
23. Moore JE, Orenstein J. 2010. *Phys. Rev. Lett.* 105:026805
24. Sodemann I, Fu L. 2015. *Phys. Rev. Lett.* 115:216806
25. Morimoto T, Zhong S, Orenstein J, Moore JE. 2016. *Phys. Rev. B* 94:245121
26. Sipe JE, Shkrebtii AI. 2000. *Phys. Rev. B* 61:5337–52
27. Young SM, Rappe AM. 2012. *Phys. Rev. Lett.* 109:116601
28. Young SM, Zheng F, Rappe AM. 2012. *Phys. Rev. Lett.* 109:236601
29. Cook AM, Fregoso BM, De Juan F, Coh S, Moore JE. 2017. *Nat. Commun.* 8:14176
30. Morimoto T, Nagaosa N. 2016. *Sci. Adv.* 2:e1501524

31. Nagaosa N, Morimoto T. 2017. *Adv. Mater.* 29:1603345
32. Fei R, Tan LZ, Rappe AM. 2020. *Phys. Rev. B* 101:045104
33. de Juan F, Grushin AG, Morimoto T, Moore JE. 2017. *Nat. Commun.* 8:15995
34. Hosur P. 2011. *Phys. Rev. B* 83:035309
35. Chang G, Xu SY, Wieder BJ, Sanchez DS, Huang SM, et al. 2017. *Phys. Rev. Lett.* 119:206401
36. de Juan F, Zhang Y, Morimoto T, Sun Y, Moore JE, Grushin AG. 2020. *Phys. Rev. Res.* 2:012017(R)
37. Nielsen HB, Ninomiya M. 1981. *Phys. Lett. B* 105:219–23
38. Chan CK, Lindner NH, Refael G, Lee PA. 2017. *Phys. Rev. B* 95:041104
39. Flicker F, de Juan F, Bradlyn B, Morimoto T, Vergniory MG, Grushin AG. 2018. *Phys. Rev. B* 98:155145
40. Tang P, Zhou Q, Zhang SC. 2017. *Phys. Rev. Lett.* 119:206402
41. Sanchez DS, Belopolski I, Cochran TA, Xu X, Yin JX, et al. 2019. *Nature* 567:500–5
42. Takane D, Wang Z, Souma S, Nakayama K, Nakamura T, et al. 2019. *Phys. Rev. Lett.* 122:076402
43. Schröter NB, Pei D, Vergniory MG, Sun Y, Manna K, et al. 2019. *Nat. Phys.* 15:759–65
44. Avdoshkin A, Kozii V, Moore JE. 2019. *Phys. Rev. Lett.* 124:196603
45. Nair RR, Blake P, Grigorenko AN, Novoselov KS, Booth TJ, et al. 2008. *Science* 320:1308
46. Plank H, Pernul J, Gebert S, Danilov SN, König-Otto J, et al. 2018. *Phys. Rev. Mater.* 2:024202
47. Bel'kov VV, Olbrich P, Tarasenko SA, Schuh D, Wegscheider W, et al. 2008. *Phys. Rev. Lett.* 100:176806
48. Ganichev SD, Ivchenko EL, Prettl W. 2002. *Phys. E: Low-dimensional Syst. Nanostruct.* 14:166–171
49. Olbrich P, Karch J, Ivchenko EL, Kamann J, März B, et al. 2011. *Phys. Rev. B* 83:165320
50. Weber W, Golub LE, Danilov SN, Karch J, Reitmaier C, et al. 2008. *Phys. Rev. B* 77:245304
51. Xu SY, Ma Q, Gao Y, Kogar A, Zong A, et al. 2020. *Nature* 578:545–49
52. Ma Q, Xu SY, Shen H, MacNeill D, Fatemi V, et al. 2019. *Nature* 565:337–42
53. Olbrich P, Golub L, Herrmann T, Danilov S, Plank H, et al. 2014. *Phys. Rev. Lett.* 113:096601
54. Rees D, Manna K, Lu B, Morimoto T, Borrmann H, et al. 2020. *Sci. Adv.* 6:eaba0509
55. Ma Q, Xu SY, Chan CK, Zhang CL, Chang G, et al. 2017. *Nat. Phys.* 13:842–47
56. Osterhoudt GB, Diebel LK, Gray MJ, Yang X, Stanco J, et al. 2019. *Nat. Mater.* 18:471–75
57. Wu L, Patankar S, Morimoto T, Nair NL, Thewalt E, et al. 2017. *Nat. Phys.* 13:350–55
58. Patankar S, Wu L, Lu B, Rai M, Tran JD, et al. 2018. *Phys. Rev. B* 98:165113
59. Fiebig M, Pavlov VV, Pisarev RV. 2005. *J. Opt. Soc. Am. B* 22:96–118
60. Denev SA, Lummen TTA, Barnes E, Kumar A, Gopalan V. 2011. *J. Am. Ceram. Soc.* 94:2699–727
61. Torchinsky DH, Hsieh D. 2017. In *Rotational Anisotropy Nonlinear Harmonic Generation*, ed. CSSR Kumar, pp. 1–49. Berlin/Heidelberg: Springer
62. Zhao L, Torchinsky D, Harter J, de la Torre A, Hsieh D. 2018. In *Encyclopedia of Modern Optics*, ed. BD Guenther, DG Steel, pp. 207–26. Oxford, UK: Elsevier. 2nd ed.
63. Jackson JD. 1999. *Classical Electrodynamics*. New York: Wiley
64. Boyd RW. 2008. *Nonlinear Optics*. London: Academic
65. Pershan PS. 1963. *Phys. Rev.* 130:919–29
66. Kirilyuk A, Rasing T. 2005. *J. Opt. Soc. Am. B* 22:148–67
67. Wang Y, Xiao J, Yang S, Wang Y, Zhang X. 2019. *Opt. Mater. Express* 9:1136–49
68. Torchinsky DH, Chu H, Qi T, Cao G, Hsieh D. 2014. *Rev. Sci. Instrum.* 85:083102
69. Harter JW, Niu L, Woss AJ, Hsieh D. 2015. *Opt. Lett.* 40:4671–74
70. Sa D, Valentí R, Gros C. 2000. *Eur. Phys. J. B: Condens. Matter Complex Syst.* 14:301–5
71. Hatch DM, Stokes HT. 2003. *J. Appl. Crystallogr.* 36:951–52
72. King-Smith RD, Vanderbilt D. 1993. *Phys. Rev. B* 47:1651–54
73. Resta R. 1993. *Europhys. Lett. (EPL)* 22:133–38
74. Petersen JC, Caswell MD, Dodge JS, Sergienko IA, He J, et al. 2006. *Nat. Phys.* 2:605–8
75. Sergienko IA, Curnoe SH. 2003. *J. Phys. Soc. Jpn.* 72:1607–10
76. Yamaura JI, Hiroi Z. 2002. *J. Phys. Soc. Jpn.* 71:2598–600
77. Weller MT, Hughes RW, Rooke J, Knee CS, Reading J. 2004. *Dalton Trans.* 2004:3032–41
78. Jin R, He J, Thompson JR, Chisholm MF, Sales BC, Mandrus D. 2002. *J. Phys.: Condens. Matter* 14:L117–23
79. Hiroi Z, Hanawa M, Muraoka Y, Harima H. 2003. *J. Phys. Soc. Jpn.* 72:21–24

80. Vyaselev O, Arai K, Kobayashi K, Yamazaki J, Kodama K, et al. 2002. *Phys. Rev. Lett.* 89:017001
81. Fu L. 2015. *Phys. Rev. Lett.* 115:026401
82. Harter JW, Zhao ZY, Yan JQ, Mandrus DG, Hsieh D. 2017. *Science* 356:295–99
83. Harter JW, Kennes DM, Chu H, de la Torre A, Zhao ZY, et al. 2018. *Phys. Rev. Lett.* 120:047601
84. Bousquet E, Dawber M, Stucki N, Lichtensteiger C, Hermet P, et al. 2008. *Nature* 452:732–36
85. Oh YS, Luo X, Huang FT, Wang Y, Cheong SW. 2015. *Nat. Mater.* 14:407–13
86. Di Matteo S, Norman MR. 2017. *Phys. Rev. B* 96:115156
87. Shi Y, Guo Y, Wang X, Princep AJ, Khalyavin D, et al. 2013. *Nat. Mater.* 12:1024–27
88. Padmanabhan H, Park Y, Puggioni D, Yuan Y, Cao Y, et al. 2018. *Appl. Phys. Lett.* 113:122906
89. Laurita NJ, Ron A, Shan JY, Puggioni D, Koocher NZ, et al. 2019. *Nat. Commun.* 10:3217
90. Lei S, Gu M, Puggioni D, Stone G, Peng J, et al. 2018. *Nano Lett.* 18:3088–95
91. Fujioka J, Doi A, Okuyama D, Morikawa D, Arima T, et al. 2015. *Sci. Rep.* 5:13207
92. Cao Y, Wang Z, Park SY, Yuan Y, Liu X, et al. 2018. *Nat. Commun.* 9:1547
93. Haeni JH, Irvin P, Chang W, Uecker R, Reiche P, et al. 2004. *Nature* 430:758–61
94. Schlom DG, Chen LQ, Eom CB, Rabe KM, Streiffer SK, Triscone JM. 2007. *Annu. Rev. Mater. Res.* 37:589–626
95. Verma A, Raghavan S, Stemmer S, Jena D. 2015. *Appl. Phys. Lett.* 107:192908
96. Jang HW, Kumar A, Denev S, Biegalski MD, Maksymovych P, et al. 2010. *Phys. Rev. Lett.* 104:197601
97. Haislmaier RC, Engel-Herbert R, Gopalan V. 2016. *Appl. Phys. Lett.* 109:032901
98. Ahadi K, Galletti L, Li Y, Salmani-Rezaie S, Wu W, Stemmer S. 2019. *Sci. Adv.* 5:eaaw0120
99. Russell R, Ratcliff N, Ahadi K, Dong L, Stemmer S, Harter JW. 2019. *Phys. Rev. Mater.* 3:091401
100. Ron A, Zoghlin E, Balents L, Wilson SD, Hsieh D. 2019. *Nat. Commun.* 10:1654
101. Shan J-Y, de la Torre A, Laurita NJ, Zhao L, Dashwood CD, et al. 2020. *Phys. Rev. Res.* 2:033174
102. Powell GD, Wang JF, Aspnes DE. 2002. *Phys. Rev. B* 65:205320
103. Bauer KD, Hingerl K. 2017. *Opt. Express* 25:26567–80
104. Xu T, Morimoto T, Moore JE. 2019. *Phys. Rev. B* 100:220501